Nuclear Inst. and Methods in Physics Research, A 959 (2020) 163509

Contents lists available at ScienceDirect

Nuclear Inst. and Methods in Physics Research, A

journal homepage: www.elsevier.com/locate/nima

Simulation and implementation of multiplexing modes on cold-neutron triple-axis spectrometer SIKA

Guochu Deng *, Garry J. McIntyre

Australian Centre for Neutron Scattering, Australian Nuclear Science and Technology Organisation, New Illawarra Road, Lucas Heights, NSW 2234, Australia

ARTICLE INFO

Keywords:
Multiplexing mode
Triple axis spectrometer
UBmatrix
Phonon dispersion

ABSTRACT

SIKA, a high-flux cold-neutron triple-axis spectrometer at the open-pool Australian lightwater reactor (OPAL) at the Australian Nuclear Science and Technology Organisation (ANSTO), is equipped with a 13-blade analyser and position-sensitive detector. This multiplexing design endows SIKA high flexibility to run in both traditional triple-axis and multiplexing analyser modes. In this study, two different multiplexing modes on SIKA are simulated using Monte Carlo ray-tracing methods. The simulation results demonstrate SIKA's capabilities to work in these operational modes, especially, the multi-$\boldsymbol{Q}$ const-E_f mode, where $\boldsymbol{Q}$ is the scattering wavevector and E_f is the final neutron energy. This capability was demonstrated by measuring the phonon dispersion of a Pb single-crystal sample with the multi-$\boldsymbol{Q}$ const-E_f mode on SIKA. Compared to the traditional and multi-analyser triple-axis spectrometers, multiplexing modes on SIKA combine the advantages of the high data-acquisition efficiency and flexibility to focus on local areas of interest in the momentum-energy transfer space, namely, the ($\boldsymbol{Q}$, $\hbar\omega$) space.

1. Introduction

A triple-axis spectrometer (TAS) is a powerful tool to investigate quasi-particle dynamics in condensed matter, such as phonon and magnon excitations. Most of TASs currently used follow a traditional design, which uses a single detector (see Fig. 1(a)) and only allows exploration of ($\boldsymbol{Q}$, $\hbar\omega$) space point by point. Since only a small fraction of the scattered beam is detected at one point, this design is highly inefficient in data acquisition, especially when the ($\boldsymbol{Q}$, $\hbar\omega$) space of interest is large.

In recent years, many efforts have been made to design and build new types of TAS to allow measurements at a series of points in ($\boldsymbol{Q}$, $\hbar\omega$) space simultaneously (see Fig. 1(b)) [1–5]. Some instruments have been built by introducing a so-called multiplexing analyser equipped with a position-sensitive detector (PSD). In such a design, the traditional analyser with an array of crystals is substituted by a series of analyser blades. Each blade on the multi-blade analyser is able to rotate independently to any specific angle, which allows detectors to collect the scattered neutrons over a large range of reciprocal space ($\boldsymbol{Q}$) or energy transfer ($\hbar\omega$) at the same time. Thus, each analyser blade corresponds to a signal channel, which substantially improves the data acquisition efficiency. In order to avoid cross-talk between neighbouring signal channels, normally, radial pre-analyser and pre-detector collimators are included. RITA-I at Risø [2], RITA-II [6] at Paul Scherrer Institute (PSI), BT-7 [7] and SPINS [8] at NIST Centre for Neutron Research are typical examples of the unconventional multiplexing analyser TAS. Another type of design to improve the data-acquisition efficiency is the multi-analyser/detector system, in which there is a series of independent analysers and detectors, arranged in the scattering plane and covering a quite large scattering angle. In this design, normally, the analyser and detector are designed for a few fixed final energies, which sacrifices the flexibility. For example, the FLATCONE option [3] for IN8, ThALES and IN20 at the Institute Laue-Langevin (ILL) consists of 31 analyser channels, covering a scattering angle range of 75°. Not only can two different final energies ($\boldsymbol{E}_f$ = 1.5 Å^{-1} and 3 Å^{-1}) be chosen for experiments, but also the whole detector system can be tilted to collect out-of-plane data in momentum space. MultiFLEXX is another multi-analyser TAS at Helmholtz-Zentrum Berlin (HZB) [4]. It also provides 31 analyser-detector channels covering a scattering angle range of 75°. Each analyser-detector channel consists of five independent analysers and detectors, which correspond to final energies of 2.5, 3.0, 3.5, 4.0 and 4.5 meV. This means that it is able to map a $\boldsymbol{Q}$ space at five independent energy transfers simultaneously. A new multi-analyser spectrometer CAMEA [5], which is designed for the European Spallation Source (ESS) in Lund, covers a scattering angle range of 60°. Each analyser channel has three analyser-detector sets in series.

Both multiplexing and multi-analyser TASs improve the data-acquisition efficiency, compared to a traditional single analyser /detector TAS. However, a multiplexing TAS provides more flexibility in instrument configurations and measurements while a multi-analyser

* Corresponding author.
E-mail addresses: gc.deng.ansto@gmail.com, guochu.deng@ansto.gov.au (G. Deng).

https://doi.org/10.1016/j.nima.2020.163509
Received 10 November 2019; Received in revised form 17 January 2020; Accepted 20 January 2020
Available online 23 January 2020

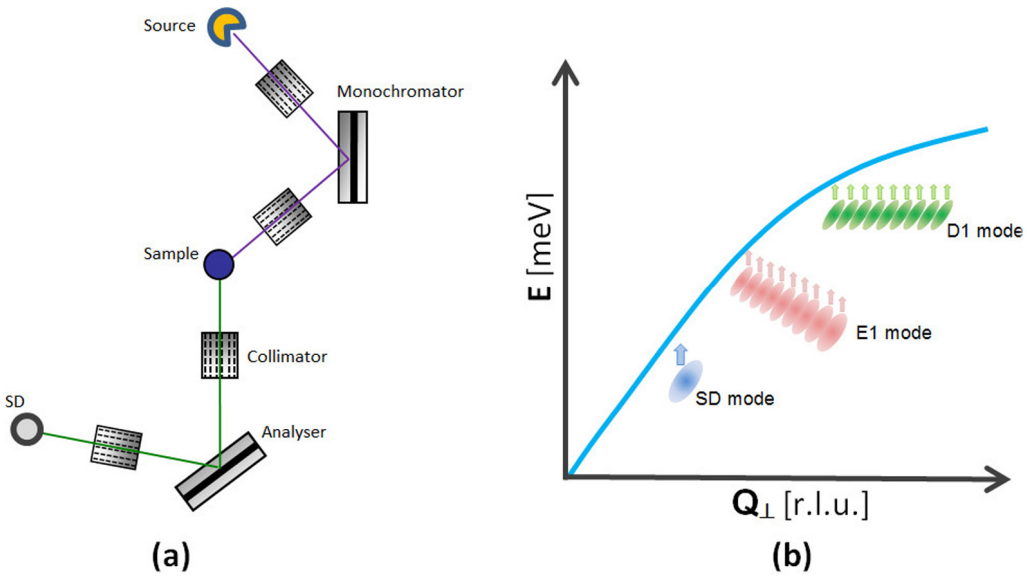

Fig. 1. (a) Traditional single-detector TAS mode; (b) Comparison of scans by using the single-detector mode, multiplexing E1 mode, and multiplexing D1 mode; The solid curve shows a dispersion curve to be measured. The blue ellipse denotes single-detector resolution, the pink ellipses denote resolutions of E1-mode channels, and the green ellipses denote resolutions of D1-mode channels. Arrows shows the scan directions. (For interpretation of the references to colour in this figure legend, the reader is referred to the web version of this article.)

TAS covers a wider $\boldsymbol{Q}$ range simultaneously. Table 1 compares the designs and advantages of the traditional and unconventional TASs.

SIKA is a high-flux RITA-type cold-neutron TAS, which is constructed at the reactor face of the open-pool Australian lightwater reactor (OPAL) of the Australian Nuclear Science and Technology Organisation (ANSTO) [9]. The design of SIKA is similar to BT-7, the double-focusing thermal-neutron TAS at NIST [7]. The secondary spectrometer of SIKA is composed of a multi-blade analyser, including 13 PG (002) blades, a linear PSD, and a separate single detector. It is able to operate in a traditional point-by-point mode by using the single detector or in different multiplexing modes with the PSD, e.g. focusing-analyser mode, q-dispersive modes, and energy-dispersive modes. Theoretically, the multiplexing operation modes could be realized in many different ways with various collimator-detector configurations. The basic idea is to extend the detecting range in the momentum or energy space with one scattering configuration by driving the analyser blades to a series of specific angles. Thus, the data acquisition efficiency can be improved due to the PSD efficiency.

In this study, we simulate the two multiplexing operation modes on SIKA by using the Monte Carlo ray-tracing technique, including the energy-dispersive flat-analyser mode (the so-called E1 mode in Ref. [10]) and the multi-$\boldsymbol{Q}$ const-$\boldsymbol{E}$ mode (the so-called D1 mode in Ref. [10]) (see Fig. 1(b)). The energy resolution of each signal channel of these modes is calculated and presented. With the D1 mode, not only has the simulation been conducted, but also an experiment was performed to measure the phonon dispersions from a Pb single crystal because the same E_f of each channel in the D1 mode simplifies the data treatment. Analysis of the real data has been conducted and presented. These simulations and experiments demonstrate the capability of multiplexing modes of SIKA, and provide a profound understanding to multiplexing design and guidelines for conducting a successful multiplexing experiment on SIKA.

2. Methods for simulations and experiments

SIKA's secondary spectrometer is installed in a cylinder-shaped chamber of an external diameter 1.5 m. The analyser stage, the pre-detector collimator and the detector system is shielded by the multi-layer shielding of B_4C and high density polyethylene (HDPE). The 13 PG analyser blades (20×180 mm^2) with independent rotations are installed on the analyser stage, which can rotate the analyser array in any specific angle. The detector system includes a single detector, a diffraction detector and a multiwire PSD, which all can move on a rail of a diameter of 800 mm around the centre of the analyser stage. The sample analyser distance is extendable, but fixed to 1960 mm for the simulation and experiment. The PSD is a 48-wire multiwire detector from Ordela. The spatial separation between two neighbour wires is around 1 cm. It roughly covers a 50° scattering angle from the central blade. The detailed drawing can be found in the SIKA instrument paper [9].

The simulations were conducted by using the Monte Carlo ray-tracing package RESTRAX by J. Šaroun [11]. The simulation has been done on a dummy incoherent single-crystal sample with a cubic structure with lattice parameter $a = 4.98$ Å, the same as the lead (Pb) sample for the experiment. The geometric configuration for the neutron source, guide, monochromator, analyser and collimators are based on the current instrument geometry of SIKA described above. The pre-monochromator and pre-sample collimators are 60′ while the pre-analyser and pre-detector collimators are 80′, which correspond to the experimental configuration for the multiplexing modes. Another all-60′ collimation configuration was also simulated, in order to compare the multiplexing mode to the most frequently used conventional TAS mode on SIKA. The single-crystal sample was modelled with the two perpendicular scattering vectors, (1 0 0) and (0 1 1) in the equatorial plane. The simulation was performed near the sample reciprocal-lattice vector $\boldsymbol{Q}$ (2 0 0), where the Pb phonon dispersions were measured in the real experiment. For the E1 mode, we chose the most-frequently-used final energy 5 meV for the simulation. The energy resolution was simulated near the elastic line. Each analyser blade was considered as an independent analyser to form a signal channel for the simulation. The difference between successive analyser blades is the angle between the scattered neutron beam and the analyser blades, which results in a series of final energies. For the D1 mode, the final energies of all blades are set to 5 meV or 8.07 meV for the two different high-order-contamination filter options. The former final energy is the most frequently used one for the Be filter. The latter final energy is one good choice when using a PG filter on SIKA.

Table 2 summarizes all the instrumental configurations for the simulation mentioned above. The mosaicity of PG crystals on the SIKA monochromator and analyser is 50′. The 60′–60′–80′–80′ collimation

Table 1
Comparison of traditional and unconventional TAS designs.

TAS type	Traditional TAS	Multiplexing TAS	Multi-analyser TAS
Data acquisition	Point by point	Multichannel	Multichannel
Covered scattering angle range	Single	~10–15°	Large (e.g. 75° for FLATCONE)
Energy channel	Single	Depending on configuration	Depending on number of analysers in each channel
Flexibility	Normal	High	Low
Cross talk	No	Depending on configuration	No
Examples	IN8, ThALES, FLEXX	RITA, RITA-II, SPINS, BT-7, SIKA	FLATCONE, MultiFLEXX, CAMEA

The cross talk in this table generally includes the spatial overlap on the PSD and other scattering signals which causes the background increase on other channels.

Table 2
Instrument configurations for simulating the E1 and D1 modes on SIKA.

Mode	Collimation	$\boldsymbol{K}_i$ (Å^{-1})	$\boldsymbol{K}_f$ (Å^{-1})	Q (r.l.u.)
E1 mode (E_f = 5.00 meV)	60′–60′–60′–60′	1.553	1.553	~(2, 0, 0)
E1 mode (E_f = 5.00 meV)	60′–60′–80′–80′	1.553	1.553	~(2, 0, 0)
D1 mode (E_f = 5.00 meV)	60′–60′–60′–60′	1.553	1.553	~(2, 0, 0)
D1 mode (E_f = 5.00 meV)	60′–60′–80′–80′	1.553	1.553	~(2, 0, 0)
D1 mode (E_f = 8.07 meV)	60′–60′–60′–60′	1.974	1.974	~(2, 0, 0)
D1 mode (E_f = 8.07 meV)	60′–60′–80′–80′	1.974	1.974	~(2, 0, 0)

corresponds to the multiplexing modes, in which the pre-analyser and pre-detector collimators are radial with 80' divergence. We also simulated the scenario with the 60′–60′–60′–60′ Söller collimation in order to compare with the single-detector mode. In reality, the single detector mode on SIKA is very similar to the case of the central blade of the multiplexing mode except that the detector is a single detector rather than a single detector wire on the PSD. Thus, the comparison between the multiplexing mode and the single detector mode can be done by the simulated result for the central blade and the results for all the blades. The data acquisition rate is about 9 times faster in the multiplexing mode than the single detector mode if 9 analyser channels in use.

A neutron experiment was conducted on a Pb single-crystal sample with the multi-$\boldsymbol{Q}$ const-$\boldsymbol{E}_f$ mode at the final energy $\boldsymbol{E}_f$ = 8.07 meV. Two 60′ Soller collimators are used for the pre-monochromator and pre-sample positions while both the pre-analyser and pre-PSD collimators are 80′ radial ones. Before starting the experiment with the sample, the monochromator and analyser angles of SIKA were calibrated with the central analyser blade by using the Bragg peaks and incoherent scattering of a nickel (Ni) powder sample. The counting efficiency of each wire in the PSD was measured and calibrated by using a polycrystalline vanadium (V) rod, which has a dimension of Φ10 mm × H45 mm. To avoid the signal from the sample holder, only the top part of the V rod (~40 mm) was in the beam. The final energy of each blade was calibrated individually by using the incoherent signal from the same V sample and rocking each blade to maximize the intensity on the PSD. The Pb single crystal was placed in air and aligned by using two independent Bragg reflections (200) and (022), which were used to build the orientation (UB) matrix [12,13]. The longitudinal and transverse phonon dispersion curves were measured for around 30 s per point near the zone centre $\boldsymbol{Q}$ (200). The data were normalized by using the V scans mentioned above. The normalized data were treated by using a Python code to generate a 3D dataset in the Q_{H}-Q_{KL}-E space.

3. Simulation results and discussions

3.1. Simulation of energy-dispersive flat-analyser mode

The instrumental configuration of the energy-dispersive E1 mode is shown in Fig. 2. As can be seen in Fig. 2(a), the analyser blades remain flat just like a traditional unfocused analyser. The most important difference between the traditional mode and the E1 operation mode is the radial collimator between sample and analyser, which separates the scattered neutron signals from the sample into 13 channels. Going through each analyser blade, the neutron beam in each channel reaches the PSD and generates signals at different areas of the PSD. Since the incident angles on the analyser blades are different, the corresponding final energy $\boldsymbol{E}_f$ at each blade is different too. This is demonstrated in Fig. 2(b) by using different colours for the 13 channels. Fig. 2(c) displays the scattering triangles of different blades in this operational mode. It is clear that the $\boldsymbol{K}_f$ angle and modulus change for different blades.

In the E1 mode, the divergence angle, δ_{i}, which is the angle between beam to the ith blade and the central blade from the sample, is given by the following equation:

$$\delta_i = \arctan\left(d_i * \sin(\frac{A_2}{2}) / \left(L_{SA} - d_i * \cos(\frac{A_2}{2})\right)\right) \quad (1)$$

where L_{SA} is the distance between sample and analyser, d_{i} the distance of the ith blade from the centre of the analyser stage, and A_2 is the take-off angle of the analyser. The diffraction angle for the ith analyser blade is $A_2/2+ \delta_{\mathrm{i}}$, which also defines $\boldsymbol{K}_f$ of the outcoming beam for this blade. The angle between $\boldsymbol{K}_i$ and $\boldsymbol{K}_f$ is $S_2 + \delta_{\mathrm{i}}$, where S_2 is the sample take-off angle. With all these geometric relationships and the Bragg law, we are able to calculate the configuration of each blade for the Monte-Carlo simulation.

From the discussion above, we consider each analyser blade as an independent analyser to calculate its resolution ellipsoid. Actually, these analyser channels look like a series of traditional TAS measurements operating at the same E_i but 13 slightly different E_f, which is schematically shown by the pink ellipses in Fig. 1(b).

All the resolution ellipsoids of the signal channels demonstrated in Fig. 2(b) are simulated for the two different collimation configurations: 60′–60′–60′–60′ and 60′–60′–80′–80′. The projections of these ellipsoids of the former configuration from the odd-numbered blades are plotted in Fig. 3(a) and (b) in the $Q_{\parallel}$-E and $Q_{\perp}$-E spaces, respectively. The similar projections of the latter one are shown in Fig. 3(c) and (d). The simulations give the momentum resolution in the $Q_{\parallel}$-$Q_{\perp}$ space as well, which is not shown here. These figures show that the final energies of all those blades cover a range from −0.6 meV to 0.5 meV compared to the final energy of the central blade. For both cases, the momentum shifts along the $Q_{\parallel}$ direction are smaller than the shifts along the $Q_{\perp}$ direction. The shaded areas in the purple ellipses in Fig. 3 indicate the full widths at half maxima (FWHM) of the resolution peak. As can be seen, the resolution ellipses in the $Q_{\parallel}$-E spaces heavily overlap each other while those resolution ellipses in the $Q_{\perp}$-E space are well separated. It is clear that the tighter collimation 60′–60′–60′–60′ improves the resolution by 15% in comparison to the wider one 60′–60′–80′–80′. Since both 60′ and 80′ are quite large divergence for a collimator, no significant count rate drop from the former was noticed. From the shaded area of the last channel, which corresponds to the FWHM of the purple ellipse on the top of each plot in Fig. 3, we are able to estimate the cross-talks between the neighbour channels for both

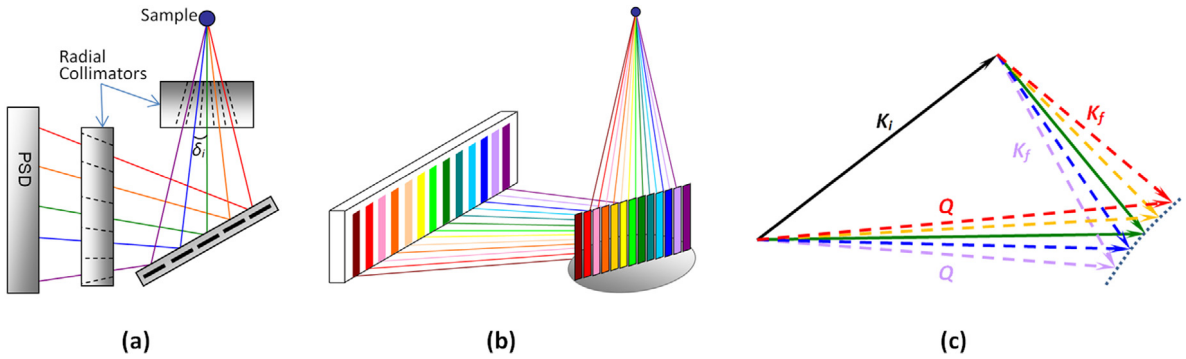

Fig. 2. (a) Schematic configuration of the analyser and detector system for the energy-dispersive flat-analyser mode (namely, the E1 mode); (b) Schematic of the scattering and data acquisition channels through all analyser blades in the E1 mode; colours on the PSD indicate the different E_f of each channel; (c) Scattering triangle of the E1 mode, where the final wavevector K_f of each neutron scattering channel varies due to different angles between sample and each analyser blade. A series of data with different $\boldsymbol{Q}$ and E_f are collected simultaneously. (For interpretation of the references to colour in this figure legend, the reader is referred to the web version of this article.)

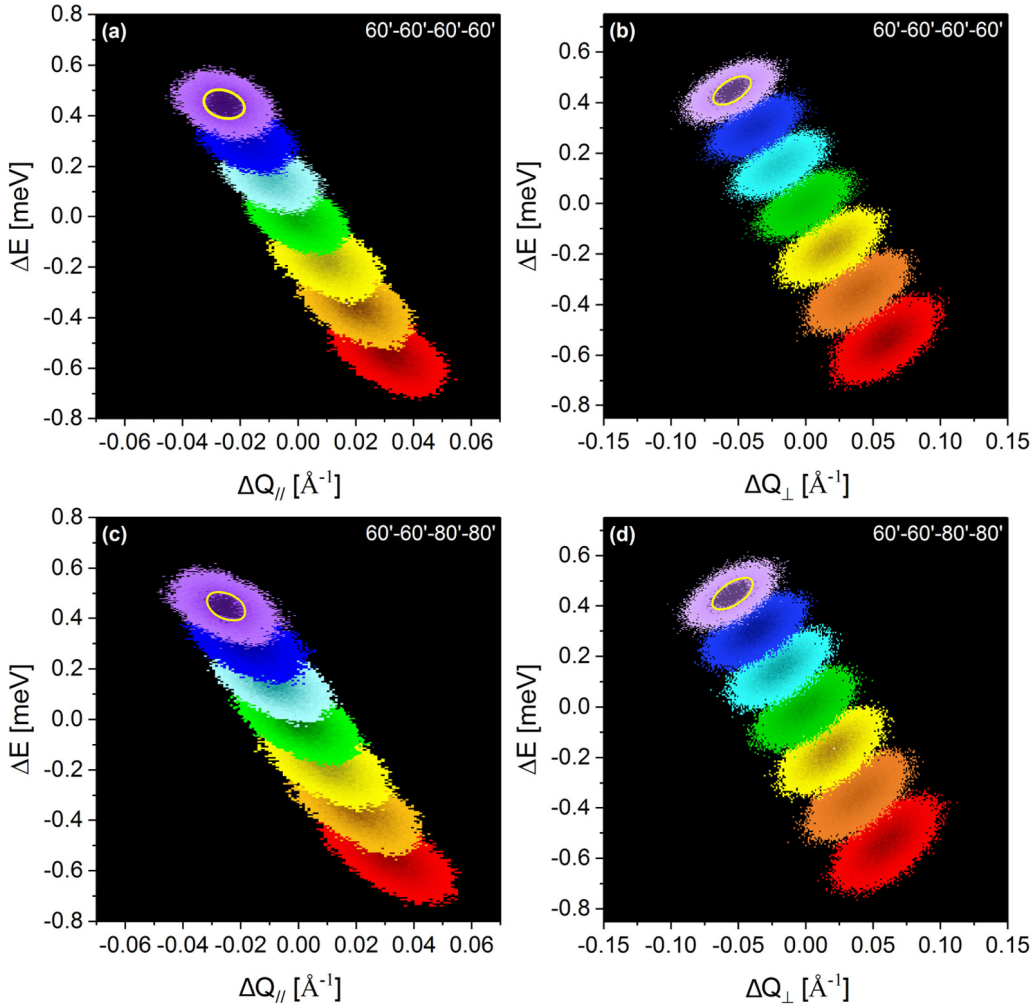

Fig. 3. Resolution ellipses of the odd-numbered analyser channels in the (a) $Q_{\parallel}$-E and (b) $Q_{\perp}$-E spaces for the E1 mode with 60′–60′–60′–60′ collimation, where ΔE = 0 and E_f = 5 meV. Similar resolution ellipses in (c) $Q_{\parallel}$-E and (d) $Q_{\perp}$-E spaces for the E1 mode with 60′–60′–80′–80′ collimation. The shaded areas with the yellow oval marks in the purple ellipses indicate the FWHM sizes of the resolution ellipses. (For interpretation of the references to colour in this figure legend, the reader is referred to the web version of this article.)

configurations. The former are better than the latter, indicating that the cross-talk can be avoided by using proper instrument configurations and collimators. Since the $\boldsymbol{K}_f$ of each signal channel is slightly different, the energy profiles of the resolution ellipses are different, too. The FWHM obtained by fitting to the simulated energy profile curves from all blades are shown in Table 3. The resolutions are slightly improved with the increase of the scattering angle, as shown in Fig. 3. The FWHM of the central blade is 0.133 meV for 60′–60′–60′–60′ and 0.148 meV for 60′–60′–80′–80′. In case of large monochromator resolution, the final instrument resolution may be dominated by the monochromator. However, this is not true in this case since our simulated final resolution still depends on the analyser. Considering the whole energy range

Table 3
Energy resolution at odd-numbered blade in of the E1 mode with different collimations.

Collimation	60′–60′–60′–60′						
Blade No.	1	3	5	7	9	11	13
FWHM (meV)	0.151(1)	0.145(1)	0.139(1)	0.134(1)	0.131(1)	0.123(1)	0.120(1)
Collimation	60′–60′–80′–80′						
Blade No.	1	3	5	7	9	11	13
FWHM (meV)	0.170(1)	0.161(1)	0.156(1)	0.148(1)	0.142(1)	0.136(1)	0.131(1)

(~1 meV) covered by all these channels, we are able to collect data over a wide energy range with high resolution in one single scan in this operational mode. This simulation demonstrates the efficiency and advantages of the multiplexing capability on SIKA.

3.2. Simulation of the multi-Q const-E_f mode

Fig. 4 shows the schematic configuration of the multi-Q const-E_f mode, namely the D1 mode. In this mode, each analyser blade rotates to a certain angle in order to fulfil the condition that all the final energies of these blades are the same (see Fig. 4(a)). Fig. 4(b) shows the total 13 signal channels corresponding to the 13 blades. Different from Fig. 2(b) for the energy-dispersive flat-analyser mode, signals on detectors in this mode have the same energy, which is shown by one single colour for all the detectors. Since the incident neutron to the sample is the same for any analyser blade, the incident energy E_i (or wave vector $\boldsymbol{K}_i$) is a constant. The final energy E_f is fixed to be the same value on each analyser blade, which means the modulus of $\boldsymbol{K}_f$ is a constant, too. As shown by the scattering triangle in Fig. 4(c), thus, $\boldsymbol{K}_f$ of each signal channel in this operational mode is the radius of a circle. In the scattering triangle, only $\boldsymbol{Q}$ and the scattering angle between $\boldsymbol{K}_i$ and $\boldsymbol{K}_f$ change for different blades. Comparing to the E1 mode, where $\boldsymbol{K}_f$ modulus and angle, and $\boldsymbol{Q}$ change at the same time, this operational mode has an advantage that the data are more straightforward and easier to be combined. The differences between the E1 and D1 operational modes are presented in the schematic of Fig. 1(b). The green ellipses of all D1 channels have the same energy transfer while the pink ones in all E1 channels have different E_f.

Fig. 5 demonstrates the Monte Carlo ray-tracing results of the projected resolution ellipses for the odd-numbered blades near the elastic line for the configurations of $E_f = 5$ meV and 8.07 meV. In this configuration, E_f is the same for all the analyser channels. Thus, all the resolution ellipses in these figures are at the same height along the E axis, while they are almost evenly distributed along the $Q_{\parallel}$ and $Q_{\perp}$ directions. It is interesting to notice that the separation between two neighbour channels is larger along the $Q_{\parallel}$ direction than that along the $Q_{\perp}$ direction. All these channels cover a range around 0.2 Å^{-1} along the $Q_{\parallel}$ direction while they cover a range around 0.1 Å^{-1} along the $Q_{\perp}$ direction. From this plot, it is obvious that the resolution ellipses along the $Q_{\parallel}$ and $Q_{\perp}$ directions at $E_f = 5.0$ meV are much smaller than those simulated for the configuration of $E_f = 8.07$ meV. Fig. 6 directly compares the energy profiles of these two final energies under two different collimation configurations. For 60′–60′–60′–60′, the FWHM of $E_f = 5$ meV is about 0.133 meV while the FWHM of $E_f = 8.07$ meV is about 0.30 meV. Both of them slightly increased in the 60′–60′–80′–80′ configuration. These simulations help to choose a proper configuration to match the resolution requirement of a real experiment with the multiplexing analyser on SIKA.

Another important feature of this operational mode is the Q range covered by the analyser blade channels, which is directly related to the subtended angle by all the blades referring to the sample position. The overall subtended angle of the blades depends on the final energy E_f, the chosen analyser stage angle, the distance from the sample, and the distance between neighbour blades. The analyser stage angle should be chosen to separate neighbour analyser channels as wide as possible. Another important condition which should be fulfilled is that any analyser blade should not be shaded by any other blades on both the incoming and outcoming beam paths. Thus, an angle around of a half of the scattering angle of E_f is quite a good choice to allow a wide coverage without shadowing effects.

4. Inelastic neutron experiment with the multi-Q const-E_f mode

In order to carry out an experiment with the multi-$\boldsymbol{Q}$ const- E_f operational mode, we should take several effects into account beforehand. First of all, the SIKA PSD has 48 counting wires, which need a calibration for the counting efficiency. Such a calibration can be done by either counting a standard V sample at a static position or scanning all the PSD wires through a Bragg peak of a standard Ni powder sample. In the current experiment, we use the latter to calibrate the counting efficiency of each wire of the SIKA PSD. Secondly, each analyser blade should be individually calibrated for the same final energy E_f. This was done by rocking each analyser blade with a standard V rod at the sample position, maximizing the intensity on the PSD.

Finally, the counting efficiency of each analyser channel could be different due to the geometric effects since the neutron flight path of each blade channel is slightly different. The neutron optics such as collimators could not be perfectly the same for each channel, too. Thus, a second efficiency calibration should be considered for the purpose of normalizing the data after the experiment. In order to do so, a standard V rod was introduced to count at the elastic line of the current operational mode with the 80' radial collimators at the pre-analyser and pre-detector positions. After calibrated by the Ni powder calibration mentioned above, the data are plotted in Fig. 7. It is worthwhile to mention that we only used 9 blades for the current commissioning experiments due to some geometric limitations, introduced by the sample position not being exactly at the geometric centre of the radical collimator after the sample. The offset is roughly about 10% of the sample-analyser distance. However, it is still possible to use 11 or even 13 blades in this mode by improving the geometric conditions in the future since we still have a few PSD wires presently not in use at both ends. As can be seen, the signals from each analyser blade primarily reach three neighbour wires and are well separated from the signals from other blades. The separation of the signal channels is very important for the current operational mode, otherwise, the crosstalk of neighbour channels could ruin the real signals from the sample. The crosstalk for a similar operational mode on RITA-II was discussed by Bahl et al. [6]

In the current experiment, we collected the data from the Pb single crystal along the longitudinal and transverse directions at room temperature. In order to test the crosstalk of each analyser channels, we carried out the longitudinal scans without and with the pre-PSD collimator, which are shown in Fig. 8(a) and (b), respectively. As clearly shown in these two figures, the signals on the PSD without the collimator show some spurious signals in comparison to the data with the collimator, especially at the low-wavevector range. This indicates that the crosstalk is a critical issue when operating a multiplexing mode. In the case without collimator, each analyser blade can form different channels together with other wires on the PSD, namely, $E_f \neq 8.07$ meV. Consequently, Bragg peak or low energy phonon signals from the sample can be caught in these undesired channels, which overlap with the signals coming from the proper channel of $E_f = 8.07$ meV. With a collimator between the analyser and PSD, these undesired channels are blocked and the crosstalk background is completely suppressed.

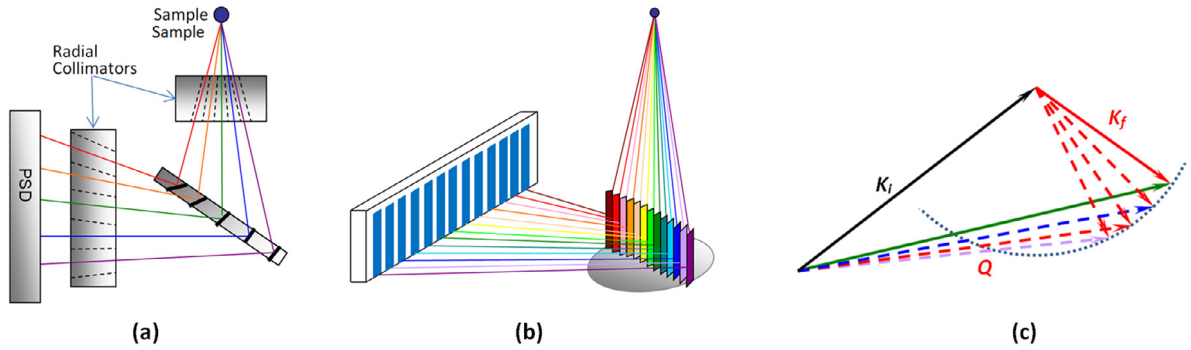

Fig. 4. (a) Configuration of the analyser and detector for the multi-Q const-E_f mode (the so-called D1 mode); (b) Schematics of neutron path from the sample through each analyser blade to the PSD in the D1 mode; (c) Scattering triangle of the multi-Q const-E_f mode, where the final energy is constant while Q varies from one analyser blade channel to the other, allowing acquisition of data in several Q channels simultaneously. (For interpretation of the references to colour in this figure legend, the reader is referred to the web version of this article.)

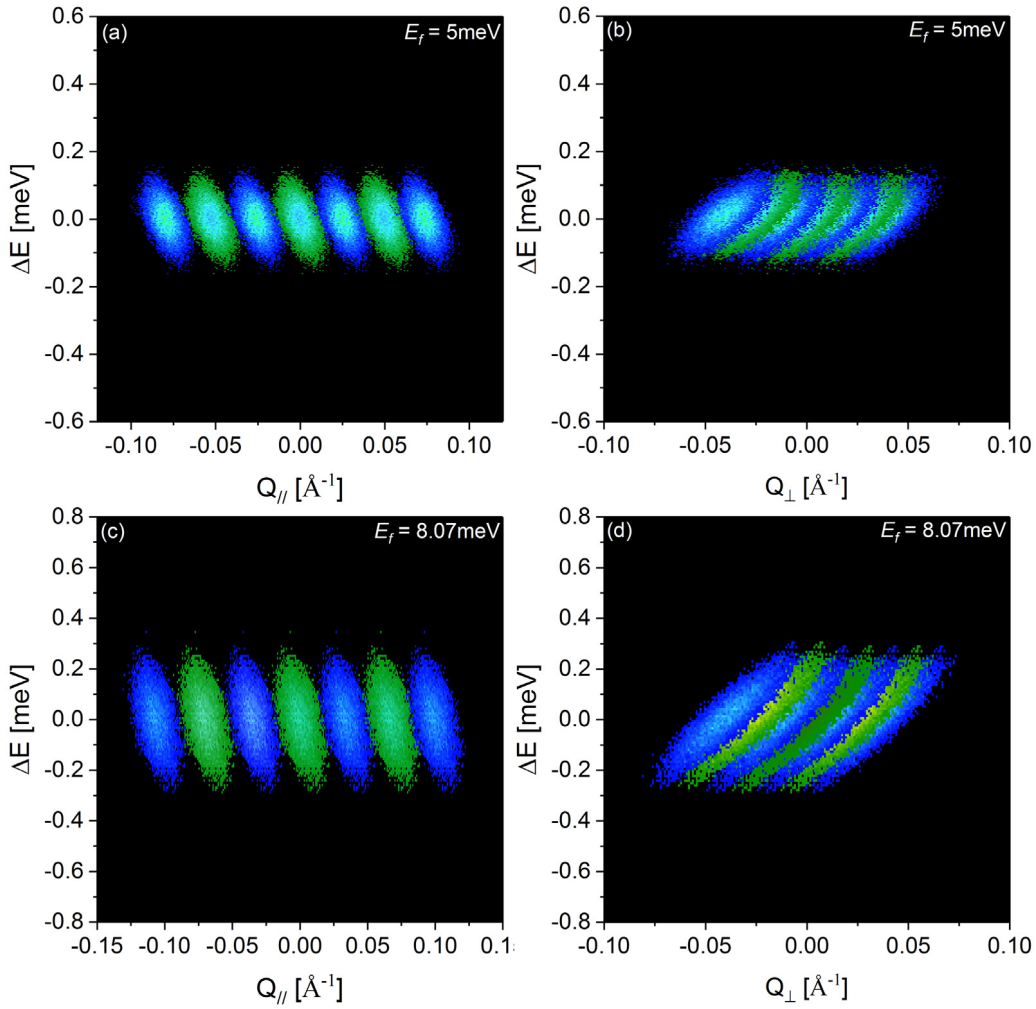

Fig. 5. The resolution ellipses of the odd-numbered analyser channels in the (a) $\boldsymbol{Q}_\parallel$-E and (b) $\boldsymbol{Q}_\perp$-E spaces for the D1 mode at $\Delta E = 0$ and $E_f = 5$ meV, and the resolution ellipses of the odd-numbered analyser channels in the (c) $\boldsymbol{Q}_\parallel$-E and (d) $\boldsymbol{Q}_\perp$-E spaces for the D1 mode when $\Delta E = 0$ and $E_f = 8.07$ meV. The two colours were used for the ellipses in order to visually distinguish the two neighbour ellipses. (For interpretation of the references to colour in this figure legend, the reader is referred to the web version of this article.)

An additional evidence to demonstrate that the collimator is highly effective to suppress the background is the comparison of the signal and background levels of these two setups. The background level of the data collected with the collimator is about 20% of the background without collimator, while the signal intensity from the former is about 50% of the signal from the latter. This is somewhat a quantitative comparison between these two configurations. It is worthwhile to point out that the lower branch in Fig. 8(a) and (b) could be from the transverse phonon signal of the slightly misaligned second grain of the Pb sample.

Fig. 8(b) and (c) show the Pb-crystal phonon-dispersion data collected along longitudinal and transverse directions, using this multi-$\boldsymbol{Q}$ mode. These data have been normalized by considering the geometric effect mentioned above. The data have also been converted from the real space into the reciprocal space according to the orientation (UB)

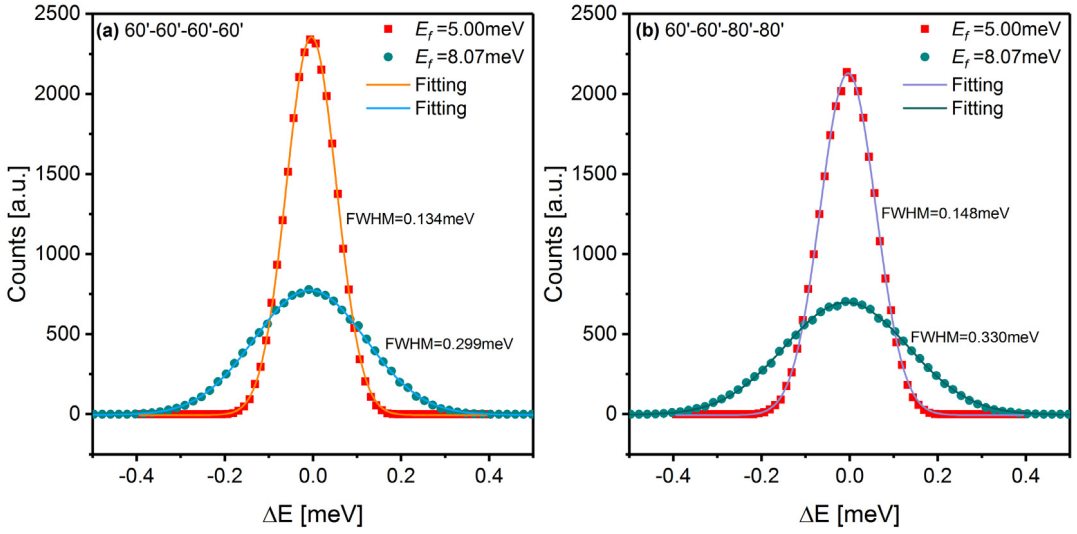

Fig. 6. Energy resolution comparison of the central blade in the D1 mode for $E_f = 5$ meV and $E_f = 8.07$ meV with 60′–60′–60′–60′ collimation (a) and 60′–60′–80′–80′ collimation (b).

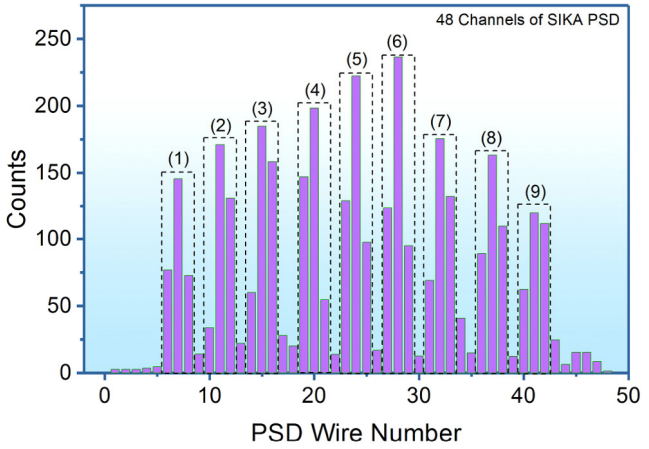

Fig. 7. The signals collected on the PSD wires with a standard V sample rod at the sample position with the multi-**Q** const-E_f mode configuration. The peak intensity was used to normalize the intensity of each channel in this mode. The dash-line boxes indicate the different analyser channels.

matrix [12,13] built during the experimental setup. As can be seen, the 9 channels in the current setup cover about (−0.06, 0.06) r.l.u. (reciprocal lattice unit) along the Q_{H} directions and about (−0.032, 0.032) r.l.u. along Q_{KL} directions. Thus, only five scans give us a full map of the longitudinal phonon branch of our Pb single-crystal with 45 individual **Q** points. However, due to the geometric setup, these points are not exactly located in the $Q_{\mathrm{KL}} = 0$ plane, but with a small Q_{KL} component limited in (−0.035, 0.035) r.l.u., and even smaller range at high-energy transfer. Along the transverse direction, the 9 channels covered a slightly smaller Q_{KL} range in one scan, especially at the higher-energy regime. This can be clearly seen from the gap between the two scans in Fig. 8(c). In this Pb phonon measurement, one scan covers about (−0.035, 0.035) r.l.u. range in Q_{KL} while it covers (−0.057, 0.057) r.l.u. along the Q_{H} direction. These results are consistent with the simulated results presented in Fig. 5. It is found that the multi-**Q** const-E_f mode can cover a wider **Q** range when measuring along the longitudinal $Q_{\parallel}$ direction than along the transverse ($Q_{\perp}$) direction. The perpendicular component is normally quite small, which may be ignored for experiments not requiring high accuracy.

It is interesting to compare the current operation mode with the traditional single-detector mode on SIKA. Normally, a Söller collimator of the same divergence rather than a radial collimator is used on the pre-analyser position, and only the central blade (~20 mm in width)

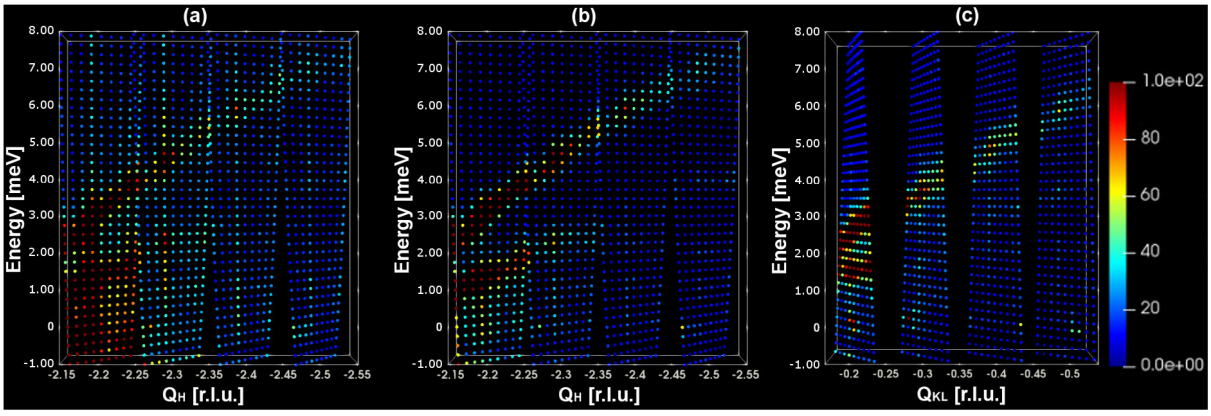

Fig. 8. (a) The phonon excitation dispersions along the longitudinal (Q_{H}) direction without the pre-detector collimator (a), along the longitudinal (Q_{H}) direction with the pre-detector collimator (b), and along the transverse (Q_{KL}) direction with pre-detector collimator (c) measured from the Pb single-crystal sample with the multi-Q const-E_f (D1) mode; The Q directions into the page are Q_{KL}(a), Q_{KL} (b) and Q_{H} (c). The intensity signals have been normalized according to the detector efficiency of each wire from the standard V scans. Both longitudinal and transverse results shown here agree well with the phonon dispersion of Pb single crystal previously reported by Brockhouse et al. [14].

will be illuminated by the scattered beam from a sample of the size about 20 mm in diameter. Thus, the broad width of the analyser is not really useful to increase the counting efficiency, especially when we use cold neutrons such as $E_f = 5$ meV or below. When we use a radial collimator at the pre-analyser position in the multi-$\boldsymbol{Q}$ const-E_f mode, each channel has similar count rate as the traditional single detector mode assuming the same sample size. Thus, the counting efficiency is 9 times faster (if we use 9 channels like in the current experiment) than the traditional single-detector system. A traditional TAS with a focused analyser should be much faster in data collection than the single blade analyser described above. On SIKA, it is possible to use multiple analyser blades to increase the counting rate in the traditional single detector mode. Such a focusing effect is more obvious for the thermal neutron range, such as $E_f = 14.87$ meV because the analyser angle θ is small (~20°) and large area of the analyser is illuminated by the scattered neutron beam. In a cold-neutron configuration, e.g. $E_f = 5$ meV, the analyser angle θ is large (~37°), and only 2 or 3 blades will be illuminated by the scattered neutron beam. We have measured the focusing effect of three focused blades on SIKA for the cold neutron case, the counting rate is around 1.5 times of a single blade.

We should also draw our attention to the comparison between the multiplexing system in this study and the multi-analyser detector system such as FLATCONE and MultiFLEXX. Actually, FLATCONE and MultiFLEXX are designed for the multi-$\boldsymbol{Q}$ const-E_f mode as we discussed above. Both of them have a series of analyser channels with the const-E_f setup. The main difference is that the analyser/detector channels of FLATCONE [3] and MultiFLEXX [4] have a scattering angle step of 2.5°, much larger than the angle step (~0.53°) in the current experiment. If we use 2.5° for the angle between the signal channels in this experiment to treat the data, we find that the $\boldsymbol{Q}$ step is much larger and one single scan will cover the Q_{H} range about ~0.25 r.l.u. and Q_{KL} range 0.39 r.l.u. The results are not shown here. Some of the data are far out of the range of interest. From this point of view, FLATCONE and MultiFLEXX are more suitable to do an overview survey experiment in the whole momentum energy space, just like a time-of-flight spectrometer, while the current multiplexing mode on SIKA is more suitable to conduct local scans near the area of interest with more detail. Therefore, both multiplexing and multi-analyser techniques substantially improve the data acquisition efficiency, and are suitable for scans of different purposes. We note that FLATCONE and MultiFLEXX cover 31 channels (covering ~75° of scattering angles), much more than 9 channels (covering ~6.5° of scattering angles) we used for comparison above, over a much larger $\boldsymbol{Q}$ range than the range shown above [3,4].

5. Conclusions

In summary, SIKA is a cold-neutron triple-axis spectrometer with the multiplexing analyser design. We discuss the two different multiplexing modes on SIKA: the energy-dispersive flat-analyser mode and the multi-$\boldsymbol{Q}$ const-E_f mode. Based on the exact SIKA geometry, Monte Carlo ray-tracing simulations have been done for both these modes and demonstrate the feasibility of these modes on SIKA. Phonon dispersion of a Pb single-crystal sample was measured on SIKA by using the multi-$\boldsymbol{Q}$ const-E_f mode. After normalization and treatment, the dispersion curve of Pb was presented in three-dimensional momentum-energy space. This experiment demonstrates the capability of SIKA in the multiplexing operation modes. Comparison between the multiplexing mode on SIKA and the multi-analyser triple axis instruments shows that the former is more suitable for detailed measurements while the latter is more suitable for large-scale surveys.

Declaration of competing interest

The authors declare that they have no known competing financial interests or personal relationships that could have appeared to influence the work reported in this paper.

CRediT authorship contribution statement

Guochu Deng: Conceptualization, Data curation, Formal analysis, Investigation, Methodology, Visualization, Writing - original draft. **Garry J. McIntyre:** Methodology, Project administration, Resources, Supervision, Validation, Writing - review & editing.

Acknowledgements

The SIKA project was financially supported by the grants from the Ministry of Science and Technology of Taiwan (MOST, Grant No.: NSC 94-2739-M008-001 and 100-2112-M-213-006-MY3). The operation of SIKA is currently funded by the National Synchrotron Radiation Research Centre (NSRRC), Taiwan. G. D cordially thanks Prof. Wen-Hsien Li (National Central University) for the leadership of SIKA design and construction, Dr. Peter Vorderwisch (Helmholtz-Zentrum Berlin für Materialien und Energie) for his in-depth discussion, Dr. Shih-Chun Chung (NSRRC) for leading the current Taiwanese neutron team, Dr. Chun-Ming Wu (NSRRC) and Dr. Shin-ichiro Yano (NSRRC) for participating the SIKA PSD commissioning, Jen-Chih Peng (NSRRC) for the SIKA PSD data acquisition support, Eno Imamovic for the SIKA design support, and Dr. Jan Šaroun (Nuclear Physics Institute, ASCR, Řež, Czech Republic) for his help with RESTRAX.

References

[1] K.N. Clausen, D.F. McMorrow, K. Lefmann, G. Aeppli, T.E. Mason, A. Schröder, M. Issikii, M. Nohara, H. Takagi, Physica B 241-243 (1997) 50.
[2] T.E. Mason, T.E. Mason, K.N. Clausen, G. Aeppli, D.F. McMorrow, J.K. Kjems, G. Aeppli, Can. J. Phys. 73 (1995) 697.
[3] M. Kempa, B. Janousova, J. Saroun, P. Flores, M. Boehm, F. Demmel, J. Kulda, Physica B (1080) (2006) 385–386.
[4] F. Groitl, R. Toft-Petersen, D.L. Quintero-Castro, S. Meng, Z. Lu, Z. Huesges, M.D. Le, S. Alimov, T. Wilpert, K. Kiefer, S. Gerischer, A. Bertin, K. Habicht, Sci. Rep. 7 (2017) 13637.
[5] F. Groitl, D. Graf, J.O. Birk, M. Markó, M. Bartkowiak, U. Filges, C. Niedermayer, C. Rüegg, H.M. Rønnow, Rev. Sci. Instrum. 87 (2016) 035109.
[6] C.R.H. Bahl, K. Lefmann, A.B. Abrahamsen, H.M. Rønnow, F. Saxild, T.B.S. Jensen, L. Udby, N.H. Andersen, N.B. Christensen, H.S. Jakobsen, T. Larsen, P.S. Häfliger, S. Streule, C. Niedermayer, Nuclear Instrum. Methods Phys. Res. 246 (2006) 452.
[7] J.W. Lynn, Y. Chen, S. Chang, Y. Zhao, S. Chi, W. Ratcliff, B.G. Ueland, R.W. Erwin, J. Res. Natl. Inst. Stand. Technol. 117 (2012) 61.
[8] S.F. Trevino, J. Res. Natl. Inst. Stand. Technol. 98 (1993) 59.
[9] C.-M. Wu, G. Deng, J.S. Gardner, P. Vorderwisch, W.-H. Li, S. Yano, J.-C. Peng, E. Imamovic, J. Instrum. 11 (2016) 10009.
[10] K. Lefmann, D.F. McMorrow, H. Ronnow, K. Nielsen, K.N. Clausen, B. Lake, G. Aeppli, Physica B 283 (2000) 343.
[11] J. Šaroun, J. Kulda, Physica B (1102) (1997) 234–236.
[12] W.R. Busing, H.A. Levy, Acta Cryst. 22 (1967) 457.
[13] M.D. Lumsden, J.L. Robertson, M. Yethiraj, J Appl. Cryst. 38 (2005) 405.
[14] B.N. Brockhouse, T. Arase, G. Caglioti, K.R. Rao, A.D.B. Woods, Phys. Rev. 128 (1962) 1099.